developed dressed interaction. We note that the extrema around $\omega_{pl}$ in $\mathrm{Re}(1/\epsilon_{q=0})$ originating from anti- and over-screening do not emerge instantaneously with carrier generation but show a delayed rise within the first 120 fs. At $t_D = 25$ fs, the spectrum is completely flat above $\hbar\omega_{pl}$, indicating bare Coulomb collisions without any screening.

The classical model for the long-wavelength and high-frequency limit of the dielectric function of an electron gas is given by Drude theory[1,32], assuming an exponential plasmon damping with a time constant $\tau$. We performed least-square fits to our data allowing $\omega_{pl}$ and $\tau$ as free parameters and keeping the lattice part fixed. Good agreement with a Drude shape is found only for late delay times with $\omega_{pl} = 14.4$ THz at $t_D = 175$ fs (see red curves in Fig. 3). $\tau$ is a measure for the memory depth of the system and for the duration of a collision. It increases from $\tau \approx 20$ fs at $t_D = 25$ fs to $\tau = 85$ fs for $t_D \geq 120$ fs. Our experimental findings support quantum kinetic theories for the nonequilibrium dynamics of the Coulomb interaction[10–14]. These models predict a delayed build-up of screening and a strongly broadened plasmon pole after ultrafast excitation. The approximate timescale for these phenomena is linked to the duration of a plasma oscillation period which is $2\pi/\omega_{pl} = 70$ fs in our experiment.

Thus, we have demonstrated a direct test for a basic concept in nonequilibrium many-body physics: the formation of dressed quasi-particles. We show that Coulomb screening and plasmon scattering are not present instantaneously after 10-fs photoexcitation of a dense electron–hole plasma in GaAs, but emerge on a timescale comparable to the inverse plasma frequency. This class of phenomena marks the earliest stage in the dynamics of strongly perturbed particle ensembles far from equilibrium. The results are obtained by applying a new technique, where the polarization response of the system to a single-cycle electric field transient covering the entire mid infrared is directly resolved. The dynamics of elementary excitations in this important spectral region can now be accessed with uncertainty-limited femtosecond resolution of both amplitude and phase. New perspectives arise for investigations in systems such as magnons in high-$T_c$ superconductors, lattice dynamics in organic semiconductors, and vibrational relaxation in large molecules and biological complexes. □

1. Mahan, G. D. *Many-Particle Physics* 2nd edn (Plenum, New York, 1993).
2. Lindhard, J. On the properties of a gas of charged particles. *Dan. Mat.-fys. Medd.* **28**, 2–57 (1954).
3. Shah, J. *Ultrafast Spectroscopy of Semiconductors and Semiconductor Nanostructures* 2nd edn (Springer, Berlin, 1999).
4. Chemla, D. S. & Shah, J. Many-body and correlation effects in semiconductors. *Nature* **411**, 549–557 (2001).
5. Osman, M. A. & Ferry, D. K. Monte Carlo investigation of the electron–hole-interaction effects on the ultrafast relaxation of hot photoexcited carriers in GaAs. *Phys. Rev. B* **36**, 6018–6032 (1987).
6. Goodnick, S. M. & Lugli, P. Effect of electron–electron scattering on nonequilibrium transport in quantum-well systems. *Phys. Rev. B* **37**, 2578–2588 (1988).
7. Young, J. F., Henry, N. L. & Kelly, P. J. Full dynamical screening calculation of hot electron scattering rates in multicomponent semiconductor plasma. *Solid State Electron.* **32**, 1567–1571 (1989).
8. Collet, J. H. Dynamical screening in the cooling theory of high-density electron–hole plasmas. *Phys. Rev. B* **39**, 7659–7665 (1989).
9. Haug, H. & Jauho, A.-P. *Quantum Kinetics in Transport and Optics of Semiconductors* (Springer, Berlin, 1996).
10. Hartmann, M., Stolz, H. & Zimmermann, R. Kinetics of screening in optically excited semiconductors. *Phys. Status Solidi B* **159**, 35–42 (1990).
11. El Sayed, K., Schuster, S., Haug, H., Herzel, F. & Henneberger, K. Subpicosecond plasmon response: Buildup of screening. *Phys. Rev. B* **49**, 7337–7344 (1994).
12. Bányai, L., Vu, Q. T., Mieck, B. & Haug, H. Ultrafast quantum kinetics of time-dependent RPA-screened coulomb scattering. *Phys. Rev. Lett.* **81**, 882–885 (1998).
13. Kwong, N.-H. & Bonitz, M. Real-time Kadanoff-Baym approach to plasma oscillations in a correlated electron gas. *Phys. Rev. Lett.* **84**, 1768–1771 (2000).
14. Vu, Q. T. & Haug, H. Time-dependent screening of the carrier–phonon and carrier–carrier interactions in non-equilibrium systems. *Phys. Rev. B* **62**, 7179–7185 (2000).
15. Schöne, W.-D. & Ekardt, W. Time-dependent screening of a positive charge distribution in metals: Excitons on an ultrashort time scale. *Phys. Rev. B* **62**, 13464–13471 (2000).
16. Köhler, H. S. Memory and correlation effects in nuclear collisions. *Phys. Rev. C* **51**, 3232–3239 (1995).
17. Camescasse, F. X. et al. Ultrafast electron redistribution through Coulomb scattering in undoped GaAs: Experiment and theory. *Phys. Rev. Lett.* **77**, 5429–5432 (1996).
18. Hügel, W. A. et al. Photon echoes from semiconductor band-to-band continuum transitions in the regime of Coulomb quantum kinetics. *Phys. Rev. Lett.* **83**, 3313–3316 (1999).
19. Bolton, S. R., Neukirch, U., Sham, L. J., Chemla, D. S. & Axt, V. M. Demonstration of sixth-order Coulomb correlations in a semiconductor single quantum well. *Phys. Rev. Lett.* **85**, 2002–2005 (2000).
20. Vu, Q. T., Haug, H., Hügel, W. A., Chatterjee, S. & Wegener, M. Signature of electron-plasmon quantum kinetics in GaAs. *Phys. Rev. Lett.* **85**, 3508–3511 (2000).
21. Bonitz, M., Lampin, J. F., Camescasse, F. X. & Alexandrou, A. Nonequilibrium plasmons in optically excited semiconductors. *Phys. Rev. B* **62**, 15724–15734 (2000).
22. Spitzer, W. G. & Fan, H. Y. Determination of optical constants and carrier effective masses of semiconductors. *Phys. Rev.* **106**, 882–890 (1957).
23. Mooradian, A. & Wright, G. B. Observation of the interaction of plasmons with longitudinal optical phonons in GaAs. *Phys. Rev. Lett.* **16**, 999–1001 (1966).
24. Abstreiter, G., Cardona, M. & Pinczuk, A. Light scattering by free carrier excitations in semiconductors. *Springer Topics Appl. Phys.* **54**, 5–150 (1984).
25. Schall, M. & Jepsen, P. U. Photoexcited GaAs surfaces studied by transient terahertz time-domain spectroscopy. *Opt. Lett.* **25**, 13–15 (2000).
26. Beard, M. C., Turner, G. M. & Schmuttenmaer, C. A. Transient photoconductivity in GaAs as measured by time-resolved terahertz spectroscopy. *Phys. Rev. B* **62**, 15764–15777 (2000).
27. Ganikhanov, F., Burr, K. C., Hilton, D. J. & Tang, C. L. Femtosecond optical-pulse-induced absorption and refractive-index changes in GaAs in the midinfrared. *Phys. Rev. B* **60**, 8890–8896 (1999).
28. Huber, R., Brodschelm, A., Tauser, F. & Leitenstorfer, A. Generation and field-resolved detection of femtosecond electromagnetic pulses tunable up to 41 THz. *Appl. Phys. Lett.* **76**, 3191–3193 (2000).
29. Wu, Q. & Zhang, X.-C. Free-space electro-optic sampling of mid-infrared pulses. *Appl. Phys. Lett.* **71**, 1285–1286 (1997).
30. Leitenstorfer, A., Hunsche, S., Shah, J., Nuss, M. C. & Knox, W. H. Detectors and sources for ultrabroadband electro-optic sampling: Experiment and theory. *Appl. Phys. Lett.* **74**, 1516–1518 (1999).
31. Fürst, C., Leitenstorfer, A., Laubereau, A. & Zimmermann, R. Quantum kinetic electron-phonon interaction in GaAs: Energy non-conserving scattering events and memory effects. *Phys. Rev. Lett.* **78**, 3733–3736 (1997).
32. Yu, P. Y. & Cardona, M. *Fundamentals of Semiconductors* (Springer, Berlin, 1996).

# On-chip natural assembly of silicon photonic bandgap crystals

**Yurii A. Vlasov**\*†, **Xiang-Zheng Bo**‡, **James C. Sturm**‡ & **David J. Norris**\*

\**NEC Research Institute, 4 Independence Way, Princeton, New Jersey 08540, USA*
† *A. F. Ioffe Physical-Technical Institute, St. Petersburg, Russia*
‡ *Department of Electrical Engineering and Center for Photonics and Optoelectronic Materials, Princeton University, Princeton, New Jersey 08544, USA*

**Photonic bandgap crystals can reflect light for any direction of propagation in specific wavelength ranges[1–3]. This property, which can be used to confine, manipulate and guide photons, should allow the creation of all-optical integrated circuits. To achieve this goal, conventional semiconductor nanofabrication techniques have been adapted to make photonic crystals[4–9]. A potentially simpler and cheaper approach for creating three-dimensional periodic structures is the natural assembly of colloidal microspheres[10–15]. However, this approach yields irregular, polycrystalline photonic crystals that are difficult to incorporate into a device. More importantly, it leads to many structural defects that can destroy the photonic bandgap[16,17]. Here we show that by assembling a thin layer of colloidal spheres on a silicon substrate, we can obtain planar, single-crystalline silicon photonic crystals that have defect densities sufficiently low that the bandgap survives. As expected from theory, we observe unity reflectance in two crystalline directions of our photonic crystals around a wavelength of 1.3 micrometres. We also show that additional fabrication steps, intentional doping and patterning, can be performed, so demonstrating the potential for specific device applications.**

The strategy behind the colloidal assembly approach is to exploit the tendency of monodisperse submicrometre spheres to sponta-
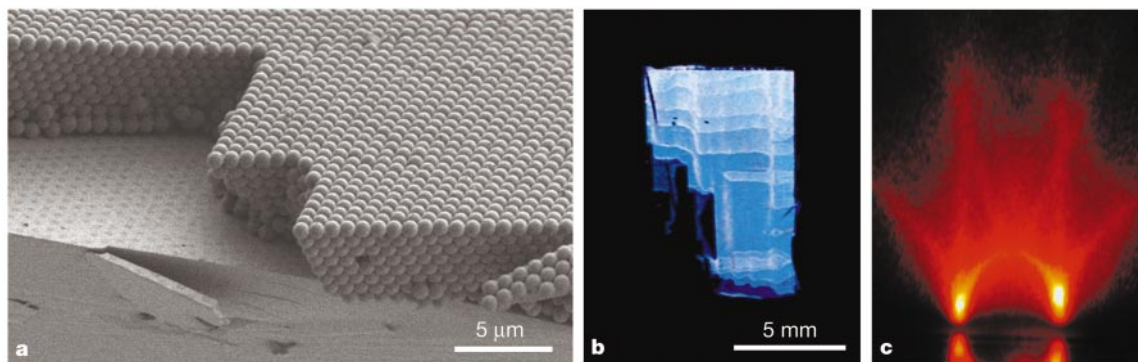
 **289**

**Figure 1** Characterization of thin planar opal templates assembled directly on a Si wafer from 855-nm spheres. **a**, Cross-sectional SEM image. **b**, Large-scale optical photograph, looking down on the wafer. The opal is formed as the meniscus is swept from right to left. The horizontal lines represent monolayer steps in the crystal (lighter shades of blue represent single-layer increases in thickness). **c**, Optical diffraction pattern obtained from the sample in **b**. Under normal incidence, a characteristic 6-spot diffraction pattern with weak Kossel rings (enhanced in the photo) remained unchanged while scanning a 100-$\mu$m-diameter laser spot over centimetre-scale regions of the opal. These 6 spots arise from diffraction off {110} planes of a single-crystal f.c.c. lattice with 1% stacking faults.

neously organize on a face-centred cubic (f.c.c.) lattice. The resulting material—a synthetic opal—acts as a template into which a semiconductor material is infiltrated. Subsequent removal of the template leads to a three-dimensional (3D) photonic crystal—inverted opal—that has periodic air-spheres embedded inside the semiconductor. If the refractive index of the semiconductor is sufficiently high (>2.85), such a structure has been predicted to exhibit a bandgap[18,19]. However the standard method for growing the initial opal (sedimentation of spheres from suspension) yields centimetre-scale pieces of polycrystalline material with numerous defects in the crystal lattice (stacking faults, dislocations and point defects). As the bandgap in f.c.c. photonic crystals is relatively narrow, these defects can easily close the gap by filling it with localized photonic states[16].

We used an alternative method to form synthetic opals. Recent research has improved control over colloidal crystallization in various geometries[20–22]. In particular, strong capillary forces at a meniscus between a substrate and a colloidal sol can induce crystallization of spheres into a 3D array of controllable thickness[22]. If this meniscus is slowly swept across a vertically placed substrate by solvent evaporation, thin planar opals can be deposited. As solvent evaporation must compete with sedimentation, this method is believed to be limited to spheres with diameters <0.4 $\mu$m. But spheres with larger diameters (~0.8 $\mu$m) are required to make photonic crystals with a bandgap at technologically important wavelengths such as 1.3 or 1.5 $\mu$m (ref. 19), so we added a convective
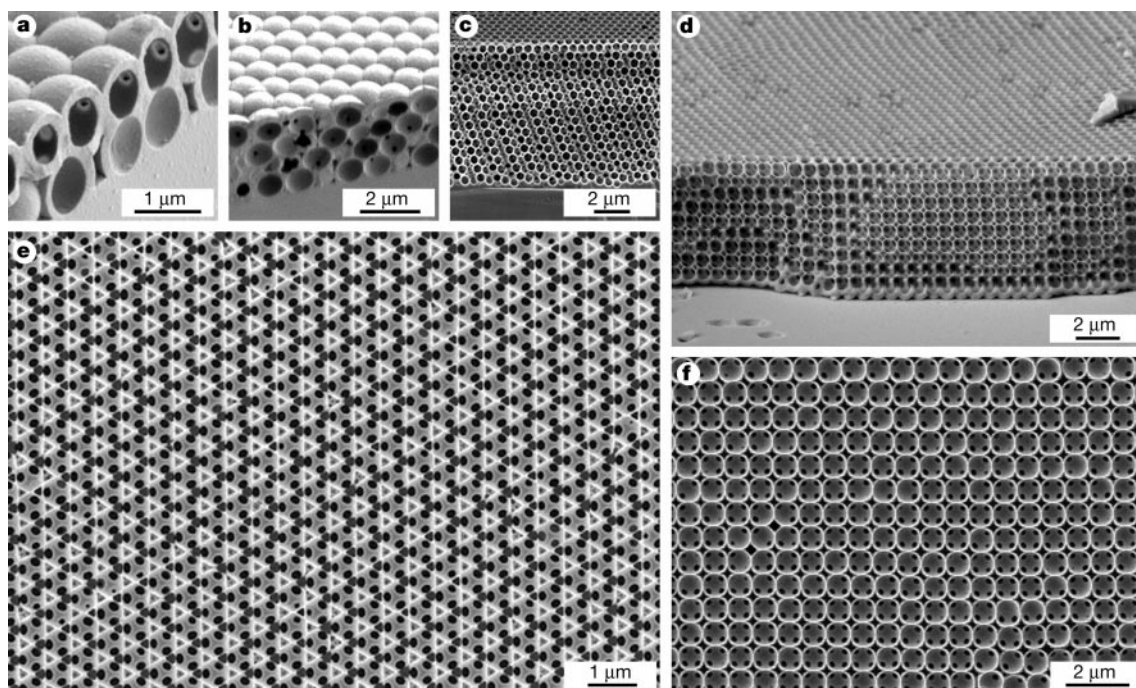


**Figure 2** SEM images of planar Si photonic crystals. Cross-sectional SEM images are shown as a function of the thickness of the initial opal template for 2 (**a**), 4 (**b**), and 16 (**c**) layers. The Si substrate is snapped, and the fracture propagates up through the photonic crystal. Close examination of the lowest layer reveals that the photonic crystals are completely integrated into the wafer. Apparent defects in **c** are due to a ripple in the fracture surface that occurs in thicker photonic crystals. **d**, Sample edge showing the (100) surface, confirming that the crystals are f.c.c. **e**, A planar (111) surface exposed by RIE. From this image, parameters[19], such as the radius of the Si coating sphere (0.41) and the radius of the air sphere (0.354), both in units of the lattice constant, were estimated. **f**, A planar (100) surface exposed by RIE. The sphere diameters are 670 nm (**c** and **e**), 855 nm (**d** and **f**), and 1 $\mu$m (**a** and **b**).

flow to the sol to minimize sedimentation and provide a continuous flow of particles toward the meniscus region. We found straightforward conditions that yielded planar opals using large (up to 1 μm) silica colloids. For example, a Si wafer was placed vertically in a vial containing an ethanolic suspension of silica spheres (855 ± 1.3% in size, 1% by volume). Flow was achieved by placing a temperature gradient across the vial (from 80 °C at the bottom to 65 °C near the top). Scanning electron microscopy (SEM) images of the resulting templates (Fig. 1a) indicate that the defect densities (~1% stacking faults, ~$10^{-3}$ point defects per unit cell) are much lower than for sedimented opals (~20% stacking faults, ~$10^{-2}$ point defects per
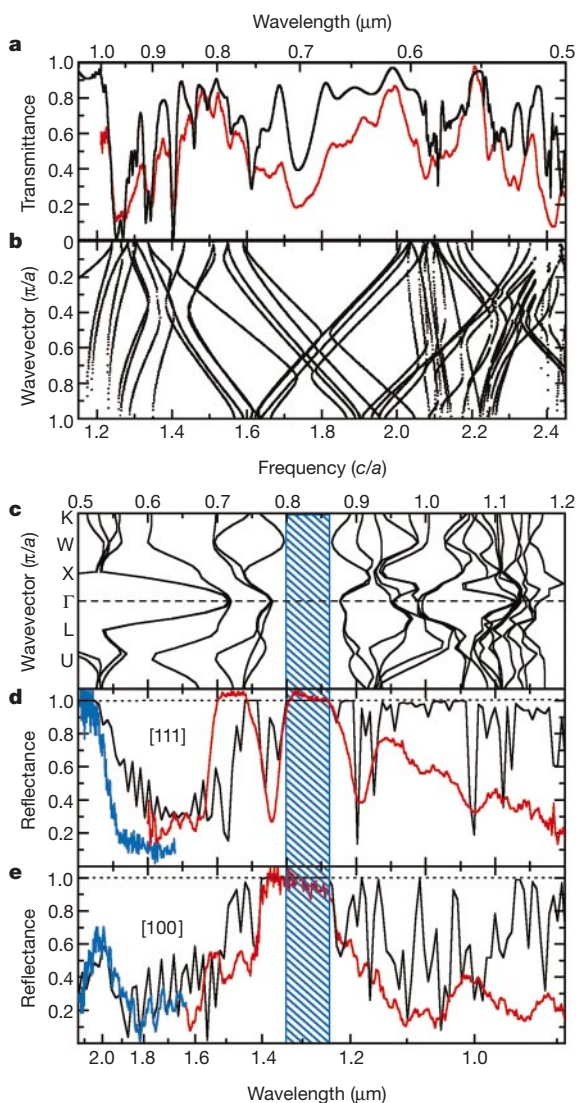


**Figure 3** Comparison of optical results with calculations. **a**, Experimental (red) and calculated (black) transmission spectra for incidence normal to the (111) plane of a 7-layer planar opal made from 855-nm silica spheres with a refractive index of 1.45. The frequency is plotted in units of $c/a$, where $c$ is the speed of light and $a$ is the lattice constant. **b**, The photonic band diagram calculated along the [111] direction for the same parameters used in **a**. **c**, The photonic band diagram calculated for the Si inverted opal measured in **d** and **e**. **d**, Experimental reflection spectra for amorphous Si inverted opals measured normal to the (111) plane. Data from two samples, with $a$ equal to 1,070 nm (red) and 841 nm (blue), are combined. The wavelength scale corresponds to the 1,070-nm sample. The best theoretical fit (black) was obtained for a Si coating sphere radius of 0.428 and an air sphere radius of 0.354. **e**, Experimental and theoretical reflection spectra as in **d** for incidence normal to the (100) plane. The blue-hatched region denotes the expected frequency range of the bandgap. For calculations, we used 12.25 as the dielectric constant of Si.

unit cell[16]). In addition, this approach yields large-sphere opals up to 20 layers thick that coat centimetre-scale areas of the Si wafer (Fig. 1b). SEM and optical diffraction measurements (Fig. 1c) show that these opals have single crystalline domains (1 mm–1 cm) that are 10–100 times larger than in the best sedimented opals. We speculate that the improved quality of these samples is due to a meniscus-induced shear that aligns the close-packed layers into a f.c.c. crystal during deposition, as shown in other geometries[23].

Once such a template was prepared, its interstitial spaces were filled with Si to satisfy the refractive index requirement for the photonic bandgap. In previous work, a purpose-built apparatus was required, in which disilane was first condensed into the pores of the opal at cryogenic temperatures and subsequently decomposed by heating at pressures of 200 torr (ref. 15). Although homogeneous infiltration was demonstrated for sedimented opals, this process did not allow sufficient control over the deposition to fill our thin planar opals. Instead, we filled planar opals using a commercially available low-pressure chemical vapour deposition (LPCVD) furnace that provides complete control of the growth parameters[24]. As LPCVD is surface-reaction-limited, this technique is in principle well suited to conformal filling of the interstitials of the opal. Furthermore, an advantage of LPCVD is that it is the standard Si deposition technique for the microelectronics industry (used, for example, in complementary metal-oxide-semiconductor, CMOS, technology). Unfortunately, under typical CMOS fabrication conditions near 600 °C, filling the opal template can be problematic. First, infiltration of the structure can be limited by premature obstruction of the outermost channels (~100 nm) of the opal, which provide gas transport to the innermost layers. Second, deposition results in polycrystalline silicon (poly-Si) with grains (~100 nm) that can introduce undesirable roughness at surfaces inside the final photonic crystal. By decreasing the temperature to 550 °C, we obtained homogeneous infiltration with LPCVD even for templates as thick as 40 layers. The lower temperature reduced the sticking coefficient of the precursor, allowing deposition to penetrate all the way to the Si wafer without a visible interface (Fig. 2a). Temperatures below 580 °C also avoided internal surface roughness by uniformly depositing amorphous silicon (a-Si), which was then transformed into a poly-Si structure with smooth interfaces by annealing at 600 °C for 8 hours. After deposition, the silica template was removed by wet etching. Thus thin planar inverted opals of controllable thickness were obtained (Fig. 2a–d) that were incorporated directly into the wafer and inherited the advantageous mechanical properties of poly-Si.

We explored the existence of the photonic bandgap in such crystals using optical spectroscopy. As structural defects can eliminate the bandgap in Si inverted opals and most defects are transferred from the template, we first examined the photonic properties of the unfilled opal (Fig. 3a and b). Figure 3b shows the photonic band diagram calculated for unfilled opals along the [111] direction of the f.c.c. lattice. The optical response of the samples was measured in the region of the higher order bands, where the diagram becomes quite complex owing to numerous interband interactions. Such experiments are important because the influence of disorder increases at higher energies where the optical wavelength becomes comparable to even small imperfections in the lattice. Further, for structures with higher refractive index the bandgap eventually develops in this region. Figure 3a shows the transmission spectrum for a 7-layer-thick opal template prepared on a transparent quartz substrate. This result, plotted on an absolute scale, was obtained with a microscope-based spectrometer attached to a two-dimensional (2D) CCD (charge-coupled device) array[25]. While the apparatus allows transmission spectra to be obtained with a spatial resolution of ~2 μm, such spectra were quite reproducible over the entire field of view of the CCD (~90 μm). When compared with calculations based on the multiple-scattering technique[26] (Fig. 3a), the experimental results reproduce the position and intensity of

all predicted spectral features up to the fiftieth photonic band (frequency ~2.4). This strongly supports the SEM evidence that the defect density in our opal templates is markedly reduced.

To perform analogous optical measurements on our Si photonic crystals, reactive ion etching (RIE) was first used to eliminate the Si coating (0.2–0.4 μm) on the top surface of the samples, which can introduce unwanted photonic surface states. By performing selective RIE before removal of the template, the silica spheres automatically terminated etching one half-layer into the crystal. Thus, a planar (111) surface, initially buried inside the structure, was exposed (Fig. 2e). Examination of the fine details in this image allowed the structural parameters of the crystal to be estimated (see Fig. 2). Using these parameters, we calculated the photonic band structure as shown in Fig. 3c[27]. The bandgap, which in inverted opals occurs between the eighth and ninth bands (the blue-hatched region in Fig. 3), was centred around 1.3 μm in our samples. To optically probe this region, we replaced the CCD in our microscope set-up with an InGaAs photodiode. Spectra were obtained (Fig. 3d and e) either by scanning the monochromator or by replacing it with a Fourier transform infrared spectrometer. Absolute reflectance was determined with an experimental accuracy of ±5% by comparing the sample reflection with that from a silver mirror. Typical reflectance spectra, measured normal to the (111) surface for 8-layer-thick samples, are presented in Fig. 3d. Near-unity reflectance is observed both in the region of the lower-order stop band (frequency ~0.5) and in the vicinity of the bandgap (frequency ~0.83) in good agreement with our calculations using the Trans-light computer code based on the transfer matrix method[28]. At higher frequencies the experimental reflectance decreases owing to the onset of absorption in Si.

The crucial test of the bandgap is to examine whether this high reflectance is maintained for directions other than [111]. Fortunately, with some effort, crystalline regions of [100] orientation can be found in our samples (Fig. 2f). Although these regions, which form near monolayer steps in the crystal[29], are very small, our microscope set-up allows their optical response to be obtained. In Fig. 3e reflection spectra are presented for such [100]-oriented regions, 8 layers thick. As in the [111] data (Fig. 3d), the bandgap region is characterized by a broad, 'square-top' reflection peak with near-unity reflectance. Furthermore, comparison of Fig. 3d and e shows that a broad range of frequencies exists around 1.3 μm where

near-unity reflectivity is maintained for both directions, as expected by theory for the bandgap. Thus, with our approach we can obtain planar Si bandgap crystals grown directly on a Si wafer.

To demonstrate the potential usefulness of these crystals, we performed two additional steps: doping and patterning. Intentional doping of the lattice with artificial defects is now possible because the concentration of native defects in our crystals is significantly reduced. Artificial defects are necessary to construct low-threshold lasers and light-emitting diodes as they can act as microcavities of high quality factor ($Q$). In comparison to 2D structures where the $Q$ of such cavities is inherently limited by the out-of-plane leakage of light, 3D bandgap crystals can completely confine the light to obtain the highest $Q$ ($>10^4$) while maintaining a diffraction-limited modal volume. In Fig. 4a, we demonstrate the first step toward creating such microcavities in our crystals. A trace amount of silica spheres of another size was added to the initial opal template before Si deposition. Consequently, an additional air cavity was introduced into one of the unit cells of the lattice. By changing the size of the dopant spheres, this cavity can be tuned to trap photons in photonic acceptor states within the bandgap. For real devices, the placement of such defects—which in Fig. 4a are randomly distributed throughout the structure—would need to be controlled. Methods to achieve this by more sophisticated assembly of the initial opal template are currently being explored.

Another step is to pattern the crystal for a specific device requirement. The planar configuration of our samples allows the possibility of using standard semiconductor microfabrication techniques, such as photolithography and RIE. As natural assembly has already defined the complex nanoscale topology of the 3D crystal, photolithography is more than sufficient to pattern the crystal into a microscale device. To demonstrate the feasibility of this idea, Fig. 4b shows an array of 100-μm-diameter 'rings' of photonic crystal that are three layers thick; the array covers a 1-mm region of the wafer. This pattern was first formed in a spun-on layer of photoresist by photolithography, and then transferred into the photonic crystal by RIE. Thicker samples can be processed by anisotropic RIE with high aspect ratios, as shown in Fig. 4c and d. Densely packed arrays of bandgap crystal devices could, in principle, be formed on a single chip. Furthermore, the technological steps required to fabricate our structures (LPCVD, oxide removal by wet etching, photolithography and RIE) are standard Si-based microfabrication techniques.
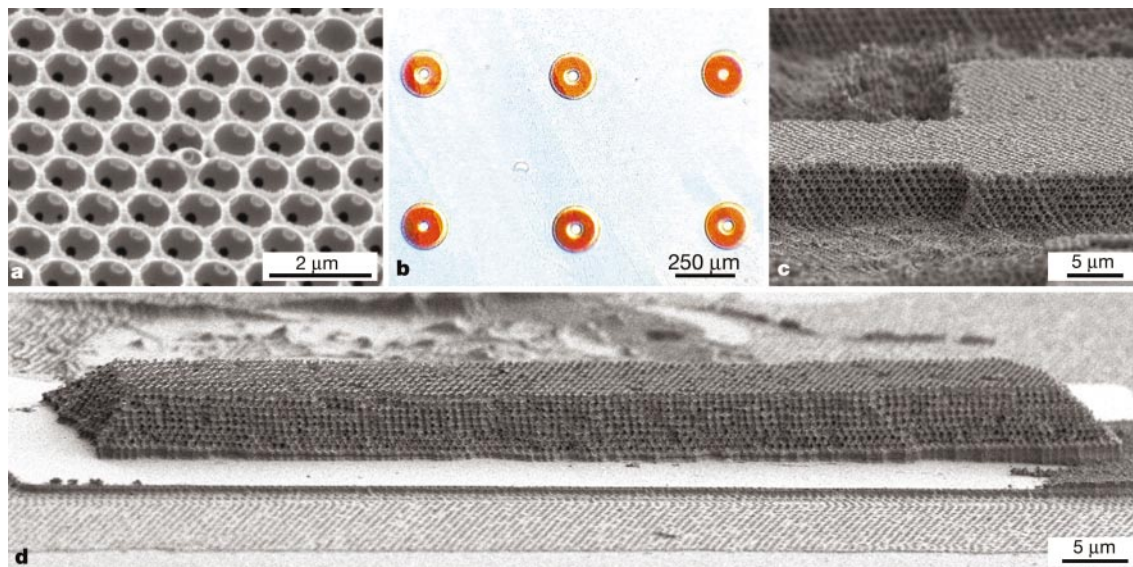


**Figure 4** Doping and patterning Si photonic crystals. **a**, SEM image showing the introduction of an interstitial defect. **b**, Photograph of an array of 100-μm photonic-crystal rings patterned into a large-area crystal via photolithography and etching. The red colour arises owing to optical diffraction from the crystal. **c**, **d**, Cross-sectional SEM images of patterned photonic crystals.

So, this approach could allow the eventual mass production of low-cost, naturally assembled, Si bandgap devices incorporated into microelectronic integrated circuits.

Such integration is desirable for adding optical functionality to current Si microelectronic devices. Devices made from planar Si bandgap crystals could allow on-chip manipulation of photons. Furthermore, the possibility of creating light in the same Si devices also exists[30]. If such an active material could be incorporated inside a high-$Q$ microcavity in our structure, a route to Si micro-lasers could be obtained. Thus, the above materials may provide an inexpensive route to all-silicon integrated optoelectronic circuits, using present-day technology. □

1. Joannopoulos, J. D., Villeneuve, P. R. & Fan, S. Photonic crystals: putting a new twist on light. *Nature* **386,** 143–149 (1997).
2. Yablonovitch, E. Inhibited spontaneous emission in solid-state physics and electronics. *Phys. Rev. Lett.* **58,** 2059–2062 (1987).
3. John, S. Strong localization of photons in certain disordered dielectric superlattices. *Phys. Rev. Lett.* **58,** 2486–2489 (1987).
4. Krauss, T. F., De La Rue, R. M. & Brand, S. Two-dimensional photonic-bandgap structures operating at near-infrared wavelengths. *Nature* **383,** 699–702 (1996).
5. Chow, E. *et al.* Three-dimensional control of light in a two-dimensional photonic crystal slab. *Nature* **407,** 983–986 (2000).
6. Smith, C. J. M. *et al.* Low-loss channel waveguides with two-dimensional photonic crystal boundaries. *Appl. Phys. Lett.* **77,** 2813–2815 (2000).
7. Painter, O. *et al.* Two-dimensional photonic band-gap defect mode laser. *Science* **284,** 1819–1821 (1999).
8. Lin, S. Y. *et al.* A three-dimensional photonic crystal operating at infrared wavelengths. *Nature* **394,** 251–253 (1998).
9. Noda, S., Tomoda, K., Yamamoto, N. & Chutinan, A. Photonic bandgap crystals at near-infrared wavelengths. *Science* **289,** 604–606 (2000).
10. Astratov, V. N. *et al.* Optical spectroscopy of opal matrices with CdS embedded in its pores: quantum confinement and photonic band gap effects. *Nuovo Cimento D* **17,** 1349–1354 (1995).
11. Wijnhoven, J. E. G. J. & Vos, W. L. Preparation of photonic crystals made of air spheres in titania. *Science* **281,** 802–804 (1998).
12. Vlasov, Y. A., Yao, N. & Norris, D. J. Synthesis of photonic crystals for optical wavelengths from semiconductor quantum dots. *Adv. Mater.* **11,** 165–169 (1999).
13. Braun, P. V. & Wiltzius, P. Electrochemically grown photonic crystals. *Nature* **402,** 603–604 (1999).
14. Müller, M., Zentel, R., Maka, T., Romanov, S. G. & Sotomayor-Torres, C. M. Photonic crystal films with high refractive index contrast. *Adv. Mater.* **12,** 1499–1503 (2000).
15. Blanco, A. *et al.* Large-scale synthesis of a silicon photonic crystal with a complete three-dimensional bandgap near 1.5 micrometres. *Nature* **405,** 437–440 (2000).
16. Vlasov, Y. A. *et al.* Manifestation of intrinsic defects in optical properties of self-organized opal photonic crystals. *Phys. Rev. E* **61,** 5784–5793 (2000).
17. Li, Z.-Y. & Zhang, Z.-Q. Fragility of photonic band gaps in inverse-opal photonic crystals. *Phys. Rev. B* **62,** 1516–1519 (2000).
18. Sözüer, H. S., Haus, J. W. & Inguva, R. Photonic bands: convergence problems with the plane-wave method. *Phys. Rev. B* **45,** 13962–13972 (1992).
19. Busch, K. & John, S. Photonic band gap formation in certain self-organizing systems. *Phys. Rev. E* **58,** 3896–3908 (1998).
20. Denkov, N. D. *et al.* Two-dimensional crystallization. *Nature* **361,** 26 (1993).
21. van Blaaderen, A., Ruel, R. & Wiltzius, P. Template-directed colloidal crystallization. *Nature* **385,** 321–324 (1997).
22. Jiang, P., Bertone, J. F., Hwang, K. S. & Colvin, V. L. Single-crystal colloidal multilayers of controlled thickness. *Chem. Mater.* **11,** 2132–2140 (1999).
23. Amos, R. M., Rarity, J. G., Tapster, P. R., Shepherd, T. J. & Kitson, S. C. Fabrication of large-area face-centered-cubic hard-sphere colloidal crystals by shear alignment. *Phys. Rev. E* **61,** 2929–2935 (2000).
24. Kamins, T. *Polycrystalline Silicon for Integrated Circuits and Displays* 2nd edn, 10–22 (Kluwer, Boston, 1998).
25. Vlasov, Y. A., Deutch, M. & Norris, D. J. Single domain spectroscopy of self-assembled photonic crystals. *Appl. Phys. Lett.* **76,** 1627–1629 (2000).
26. Stefanou, N., Yannopapas, V. & Modinos, A. Heterostructures of photonic crystals: frequency bands and transmission coefficients. *Comput. Phys. Commun.* **113,** 49–77 (1998).
27. Johnson, S. G. & Joannopoulos, J. D. Block-iterative frequency-domain methods for Maxwell's equations in a planewave basis. *Opt. Express* **8,** 173–190 (2001).
28. Bell, P. M., Pendry, J. B., Martin-Moreno, L. & Ward, A. J. A program for calculating photonic band structures and transmission coefficients of complex structures. *Comput. Phys. Commun.* **85,** 306–322 (1995).
29. Dushkin, C. D., Lazarov, G. S., Kotsev, S. N., Yoshimura, H. & Nagayama, K. Effect of growth conditions on the structure of two-dimensional latex crystals: experiment. *Colloid Polym. Sci.* **277,** 914–930 (1999).
30. Ng, W. L. *et al.* An efficient room-temperature silicon-based light-emitting diode. *Nature* **410,** 192–194 (2001).

# Smart single-chip gas sensor microsystem

**C. Hagleitner, A. Hierlemann, D. Lange, A. Kummer, N. Kerness, O. Brand & H. Baltes**

*Physical Electronics Laboratory, ETH Zurich, Hönggerberg, HPT H 6, CH-8093 Zurich, Switzerland*

..................................................................................................

**Research activity in chemical gas sensing is currently directed towards the search for highly selective (bio)chemical layer materials, and to the design of arrays consisting of different partially selective sensors that permit subsequent pattern recognition and multi-component analysis[1–3]. Simultaneous use of various transduction platforms has been demonstrated[4–6], and the rapid development of integrated-circuit technology has facilitated the fabrication of planar chemical sensors[7,8] and sensors based on three-dimensional microelectromechanical systems[9,10]. Complementary metal-oxide silicon processes have previously been used to develop gas sensors based on metal oxides[11] and acoustic-wave-based sensor devices[12]. Here we combine several of these developments to fabricate a smart single-chip chemical microsensor system that incorporates three different transducers (mass-sensitive, capacitive and calorimetric), all of which rely on sensitive polymeric layers to detect airborne volatile organic compounds. Full integration of the microelectronic and micromechanical components on one chip permits control and monitoring of the sensor functions, and enables on-chip signal amplification and conditioning that notably improves the overall sensor performance. The circuitry also includes analog-to-digital converters, and an on-chip interface to transmit the data to off-chip recording units. We expect that our approach will provide a basis for the further development and optimization of gas microsystems.**

Physisorption and bulk dissolution of analyte molecules within the polymer volume constitute the predominant interaction mechanisms of polymer-based sensors[13]. The physical properties of the polymer change on absorption of analytes: in the system we report here, these changes are detected by three distinct complementary metal-oxide silicon (CMOS) microtransducers (Fig. 1) in response to fundamentally different molecular properties of the analytes. One transducer (Fig. 1b) responds to the mass of sorbed molecules, another responds to the heat of absorption (Fig. 1c), and the third—the capacitive sensor—responds to a combination of the volume and dielectric properties of the absorbates convoluted with changes in these parameters for the sensing layer (Fig. 1a).

The capacitive sensor relies on interdigitated electrode structures, which correspond to the two plates of a standard capacitor, to monitor changes of the dielectric coefficient of the polymer. One electrode is made of the first metal layer of the CMOS process (E2 in Fig. 1a), whereas the second electrode is a stack of two metal layers (E1 in Fig. 1a). This is to enhance the sensitivity of the capacitive microsystem by increasing the number of electric field lines within the polymer volume by applying a 'three-dimensional' design[14]. The dimensions of the capacitor are $800 \times 800\,\mu m$, and its electrode width and spacing are $1.6\,\mu m$. As the nominal capacitance of the interdigitated capacitor is a few picofarads, and the expected capacitance changes on absorption of a volatile organic compound are in the attofarad range, a dedicated on-chip measurement configuration and specific signal-conditioning circuitry had to be developed. The sensor response is read out as a differential signal between a polymer-coated sensing capacitor and a passivated reference capacitor. A digital output signal is then generated by comparing the minute loading currents of both capacitors using fully differential second-order sigma-delta modulator circuitry[14]. The final output is a digital word with a precision of 20 bits.

 **293**